

RESEARCH ARTICLE

Low-power global navigation satellite system-enabled wireless sensor network for acoustic emission localisation in aerospace components

Carmine Gianni¹  | Marco Balsi¹  | Salvatore Esposito²  | Francesco Ciampa³ 

¹Department of Information Engineering, Electronics and Telecommunications (DIET), University “La Sapienza” of Rome, Rome, Italy

²Oben s.r.l., Sassari, Italy

³Department of Mechanical Engineering Sciences, University of Surrey, Guildford, UK

Correspondence

Francesco Ciampa, Department of Mechanical Engineering Sciences, University of Surrey, Guildford GU2 7XH, UK.

Email: f.ciampa@surrey.ac.uk

Summary

Structural health monitoring systems for the localisation of acoustic emission (AE) events have been developed in the past few years for aircraft components. However, these systems still require complex and heavy electrical wiring for each sensing device and sophisticated algorithms for the localisation of AE signals, which inevitably increases both weight and costs. This paper reports the creation of a low-power (few hundred mW) and low-weight (~30 g) global navigation satellite system-based wireless sensor network for the identification of AE events in aircraft structures. Each wireless node is instrumented with a low-power micro-controller, a radio frequency wireless transceiver, an analogue-to-digital converter, and a global navigation satellite system receiver for accurate time synchronisation. The AE coordinates and the speed of propagating waves are determined by using a localisation algorithm relying on time of arrival measurements. A peak amplitude detection system is implemented to process the AE data recorded by the wireless sensor network. The AE time features are locally extracted by the individual wireless modules and transferred to a remote processing unit for the execution of the localisation algorithm. Experimental results revealed that AE sources generated by low-velocity impacts are identified with a high level of accuracy. The successful implementation of the proposed wireless sensor network demonstrates its suitability for continuous and autonomous structural health monitoring aerospace applications.

KEYWORDS

acoustic emission, aerospace components, GNSS, impact localisation, wireless sensor network

1 | INTRODUCTION

Aerospace components are susceptible to low-velocity impact damage that may considerably degrade the structural integrity and, ultimately, lead to catastrophic failure. Impact events typically generate acoustic emissions (AEs)

This is an open access article under the terms of the Creative Commons Attribution-NonCommercial-NoDerivs License, which permits use and distribution in any medium, provided the original work is properly cited, the use is non-commercial and no modifications or adaptations are made.

© 2020 The Authors. Structural Control and Health Monitoring published by John Wiley & Sons Ltd

propagating into the component, which can be recorded by sparse arrays of surface bonded piezoelectric (PZT) transducers.¹⁻³ The analysis of measured AE waveforms using sophisticated impact localisation algorithms allows retrieving the location of the AE source. A number of acoustic/ultrasonic structural health monitoring (SHM) systems have been developed in the past few years for the localization of AE events in different materials and components.^{4,5} Kundu⁶ recently provided a review of AE source localisation algorithms with sparse arrays of PZT sensors. These methods typically rely on the time-of-arrival (TOA) measurements of ballistic waves originated from the impact. The most common technique used for the localisation of AE sources is the triangulation method, also known as the “Tobias algorithm,”⁷ which requires three PZT receiver transducers located at the centres of three circumferences, with the AE source identified by their geometrical intersection. Kundu et al.^{8,9} determined the impact damage by minimising an error function that used the differences of TOA from multiple AE signals. In addition, beamforming techniques such as the “Elliptical” (or “Delay-and-Sum”), “Hyperbolic,” “Energy Arrival,” and the “Reconstruction Algorithm for the Probabilistic Inspection Damage” methods have been widely used for AE detection and localisation.¹⁰⁻¹² These techniques rely on the measurement of differenced waveforms, i.e., the residual signals from the damaged and undamaged structure measured by all possible transmitter–receiver pairs. However, all of these AE methodologies require the knowledge of the group velocity of propagating elastic waves, which is difficult to obtain especially in the presence of dispersive guided modes. Ciampa and Meo¹³ overcame this issue by developing an AE source localisation algorithm in which unconstrained optimisation and the Newton–Raphson method were used to determine the impact coordinates and the group velocity of dispersive flexural modes. The same authors also proposed an alternative technique to the TOA-based method that consisted of calculating the “time reversal” operator from a baseline of signals containing the impulsive structural response of the medium.¹⁴⁻¹⁶ Recently, Ebrahimkhanlou and Salamone¹⁷ developed an AE source localisation method based on the correlation between measured waveforms with multimodal edge reflections and analytical simulations.

Nevertheless, all the above-mentioned SHM systems necessitate complex and heavy electrical wiring for each sensing device and sophisticated algorithms, which inevitably increases both weight and costs. This is against the current philosophy of SHM systems for aircraft structures requiring small, lightweight, and low-power sensing technology. As an example, the Airbus A380 has nearly 500 km of cables consisting of ~100,000 wires and ~40,000 connectors.¹⁸ By replacing current wired transducers with wireless sensor networks (WSNs), the overall weight of the aircraft can be dramatically decreased.¹⁹⁻²² Early work on WSN is from Straser and Kiremidjian,²³ who proposed the design of a low-cost wireless modular monitoring system using the Motorola 68HC11 microprocessor and the eight-channel, 16-bit, 240-Hz Harris H17188IP Sigma-Delta analogue-to-digital converter (ADC). For the wireless communication, the Proxim Proxlink MSU2 wireless modem operating in the 902- to 928-MHz Industrial, Scientific and Medical (ISM) band was used. Bennett et al.²⁴ designed a four-channel wireless sensing interface capable of measuring data from two thermometers and two thin-film strain gages using the Hitachi H8/329 8-bit microcontroller and the narrow-band 418-MHz Radiometrix wireless radio.

More recently, Casciati and Chen²⁵ developed a low-power wireless transceiver allowing multichannel and real-time data transmission based on frequency-division multiplexing. The same authors²⁶ lately designed a high-performance wireless data acquisition platform incorporating various features including flexible sensor interfaces, high-power efficiency, low-noise data acquisition, and real-time and lossless data collection.

Either batteries or energy harvesting sources can be used to power WSNs.^{27,28} Lynch and Loh²⁹ and, recently, Aygurand and Gungor³⁰ provided exhaustive reviews of WSNs for SHM applications. Chen et al.³¹ proposed a wireless SHM sensing platform for the detection of AE signals generated by fatigue cracks. Liu et al.³² and, later, Yuan et al.³³ developed a low-power (up to hundred mW) wireless digital impact monitoring system that used 24 PZT transducers and a 10-MHz crystal oscillator for the system clock in order to localise impact damage on aerospace components. Becker et al.³⁴ developed an autonomous WSN that employed crack wires and strain gauge sensors to monitor the health status of aircraft structures. Bouzid et al.³⁵ developed a wireless SHM system for the localisation of AE sources on wind turbine blades. The authors used the triangulation technique with three wireless-driven surface-bonded PZT transducers. A time conversion procedure based on the difference of the time-stamp and local arrival times of wireless units was used for the clock synchronisation. This method allowed achieving a time synchronisation accuracy up to ~1.55 μ s. However, the global navigation satellite system (GNSS) can be used to provide low-power and synchronous time clock in wireless sensor modules with a time synchronisation error of ~100 ns.³⁶⁻³⁸ Shen et al.³⁹ used GNSS-enabled technology to synchronise wireless signal acquisition units for AE localisation on pipelines. Wireless nodes were constituted of an ADC, a high-performance field programmable gate array circuit with integrated signal processing features, a digital signal processor, a GPS antenna, and a wireless communication system. Since the required

wireless transmitting distance for the AE testing was up to 10 km and the sampling rate of AE signals was nearly 10 MHz, the power demand and costs of each wireless unit were inevitably high.

Nonetheless, to the authors' knowledge, no GNSS-based wireless SHM systems for the AE source localisation on aerospace components have been developed in the literature. This paper attempts to fill this gap and proposes a low-power (few hundreds mW) and low-weight (~30 g) GNSS-enabled WSN for the identification of AE events on a 2024 aluminium alloy panel typically used for aerospace applications. Each wireless node was instrumented with a GNSS receiver for accurate time synchronisation, a radio frequency (RF) wireless transceiver, an ADC, and a low-power micro-controller (MCU). Components have been chosen consistently to meet low-power requirements. The coordinates of AE events generated by low-velocity impacts were determined using a localisation algorithm developed by Ciampa et al.^{2,13} This algorithm was here selected among those available in the literature as it does not require any prior knowledge of the mechanical properties of the host material nor the group velocity of propagating waves. A peak amplitude detection system was implemented to process the AE data recorded by the WSN and estimate the TOA. These time features were locally extracted by the individual wireless modules and transferred to the processing unit for the execution of the localisation algorithm. The layout of the paper is as follows: in Section 6, the architecture of the proposed WSN is discussed. Section 3 describes the impact localisation algorithm and the peak amplitude method to process the AE data and estimate the TOA. Section 4 provides the experimental set-up, whilst in Section 5, the impact localisation results are illustrated. Finally, conclusions of this paper are presented in Section 6.

2 | WIRELESS SENSOR NODE ARCHITECTURE

As illustrated by Yedavalli and Belapurkur,⁴⁰ a WSN for SHM applications can be potentially used in different areas of the aircraft, from the wing to the control surfaces and fuselage. According to Ciampa and Meo,¹³ four wireless sensor nodes are required for the localisation of the AE source. In the proposed WSN architecture, each single node was designed using EAGLE CAD 7.0 and includes the PZT sensor, the *processing core module*, and the *communication interface module*. Once the impact point is detected by each wireless node, the TOA information is transmitted to a remote main node (*processing unit*) to execute the localisation algorithm and estimate the coordinates of the AE source. Figure 1 shows the block diagram of the proposed WSN and the single wireless node.

The processing core module consists of a printed circuit board with dimensions 60 mm × 60 mm and weight ~30 g, which contains a 32-bit MCU (Microchip PIC32MX450F256H), a 10-bit successive approximation (SAR) ADC integrated in the MCU, a GNSS receiver (U-BLOX LEA 6T), a micro SD slot, a USB 2.0 interface, and several expansion ports where additional modules can be mounted (Figure 2a). Table 1 reports the main characteristics of the MCU. Both the micro SD slot and the USB interface were added to the board to enhance the flexibility of the wireless module. Whilst the SD card can be used to store the acquired time data for long time, the USB 2.0 connectivity provides fast data download and can be used to power the module through a battery, a power supply, or an energy harvesting device. The PZT transducer used in each wireless node is the PIC255 PI 000041371 sensor from Physik Instrumente, which has a diameter of 6.5 mm and thickness of 0.3 mm.

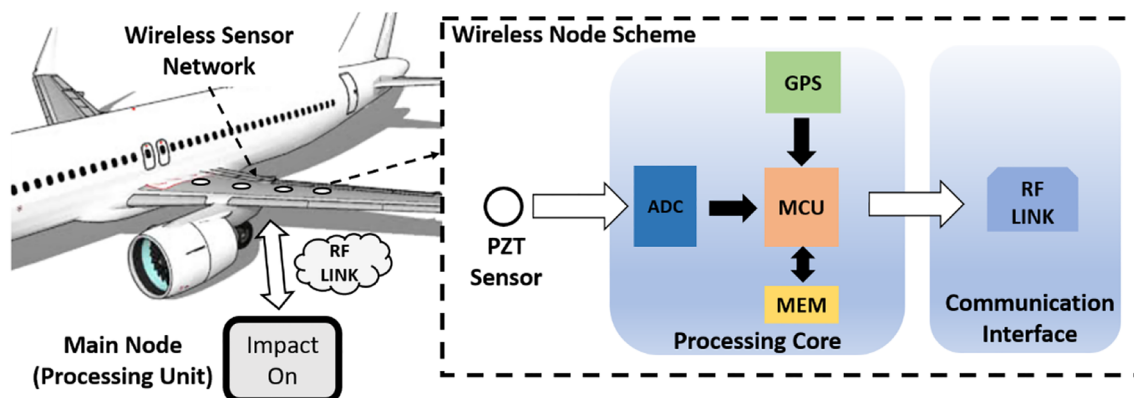


FIGURE 1 Block diagram of the single wireless node

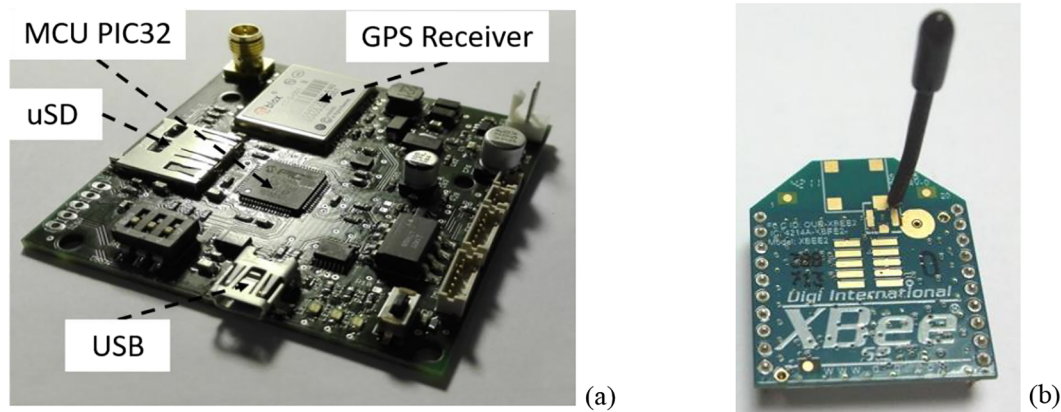


FIGURE 2 Illustration of the (a) processing core module and (b) XBEE communication (wireless) interface module

TABLE 1 Specification of the micro-controller (MCU) from microchip

MCU – PIC32MX450F256H	
Architecture	MIPS core 32 bit
Performance	120 MHz – 150 DMIPS
Flash memory	256 kB
RAM memory	128 kB

For the single wireless node, the expansion ports were connected to the communication interface RF module and to the analogue front-end. In order to match the voltage levels of the ADC (3 V), the AE waveforms measured by the PZT transducer were conditioned with an analogue front-end circuitry composed of an operational amplifier and a low-pass filter for anti-aliasing. This last element consists of a single-pole RC low-pass filter with 100 kHz cut-off frequency. The sampling rate was set at 250 kHz in order to contain sufficient information of propagating elastic waves generated by the impact event. The GNSS receiver is a U-BLOX LEA-6T GPS module designed for timing applications. Unlike other GNSS receivers, this module includes an edge detector on a pin that is synchronised with the GPS time. Once an edge is detected on the pin, the GPS receiver can be interrogated by the MCU to provide the GPS time of the edge event via a universal asynchronous receiver–transmitter interface. The GNSS receiver has also two clock outputs synchronised with GPS time that allow achieving high synchronisation accuracy in the order of 100 ns. Such time accuracy is of significant importance for the proposed impact localisation algorithm as poor time synchronisation would result in large errors for the estimation of impact coordinates. Once the impact is correctly detected, its time information is transferred by the MCU to the central processing unit through a wireless channel. The communication (wireless) module (Figure 2b) is a XBEE Series 2 operating in the 2.4-GHz ISM band that is linked to the MCU through a universal asynchronous receiver–transmitter interface. It incorporates the wireless communication ZigBee protocol with IEEE 802.15.4 standards that is used for aeronautical applications.³⁴ The transmitting RF data rate is 250 kbps with an output power of 2 mW, and its effective transmitting distance varies from 30 to 120 m in free air.

2.1 | Power budget of the wireless sensor node

Each wireless sensor node was specifically designed for low-power SHM applications with a total power consumption in the range of hundred mW. Hence, a field programmable gate array-based solution was not considered as a valuable option for the wireless architecture, as it would significantly enhance processing capabilities of the wireless module whilst increasing the power consumption.⁴¹ As for the time synchronisation, the GPS receiver requires continuous locking with the timing signals from satellites, which would inevitably affect the power performance of the wireless unit. For this reason, a low-power mode was adopted in this work, which is generally known as “sleep” (standby) mode.⁴² In the “sleep” mode, the communication (wireless) interface module is switched off when no data have to be transmitted. The lowest power is provided to all other components of the processing core module until a triggering

signal is detected from the PZT sensor. Contrarily, once an impact event is detected, the “active” mode is enabled, and the processing core wakes up and senses the AE signals. In the proposed WSN architecture, the sensor nodes are Zigbee end devices, whilst the remote central node is the Zigbee coordinator. The transmitted frame is created using the XBEE API Frame generator, and it contains the packet control data such as the “Start Delimiter,” the frame “Length,” “Type” and identification “ID,” the destination device address, and the maximum hops (radius). The “Start Delimiter” is a unique number that indicates the beginning of the data frame, whilst the frame “ID” prevents data chaos in data transmission. Table 2 reports a typical frame transmitted to the processing unit.

With reference to Table 2, the time synchronisation information is contained inside the “Data” field of the packet and consists of the following two data:

1. the GPS Time of Week that it is a word of 4 bytes containing the elapsed time in ms from the beginning of the current week;
2. the GPS Time of Week fraction of ms that it is a word of 4 bytes containing the fraction of millisecond expressed in nanoseconds of the GPS Time of Week.

The resulting TOA information obtained via synchronisation with the GPS is finally communicated by the RF unit, which switches on for a short time duration (~6 ms). Once the time-stamp is transmitted, the wireless unit returns to the “sleep” power mode. Table 3 reports the power budget of the wireless node during “active” and “sleep” modes. Figure 3 shows a diagram of the time synchronisation process with the GPS receiver and the transmission of data via the RF module.

As it can be seen from Table 3, the total power consumption of the single node is ~80 mW when no AE signal is detected and goes up to ~360 mW for few ms in order to transmit the time information to the processing unit. Such an implementation provides high flexibility to the wireless system. It also allows the proposed WSN to be powered by

TABLE 2 Typical frame transmitted from each node to the processing unit during the “active mode”

Start delimiter	Length	Type	ID	64 bit Addr.	16 bit Addr.	Radius	Options	Data
-----------------	--------	------	----	--------------	--------------	--------	---------	------

TABLE 3 Single node power requirements during “active” and “sleep” modes

	Active mode (mW)	Sleep mode (mW)
GPS	110	80
MCU	120	0.15
AMPLI	3	0.03
RF	130	0.03
TOTAL	363	80

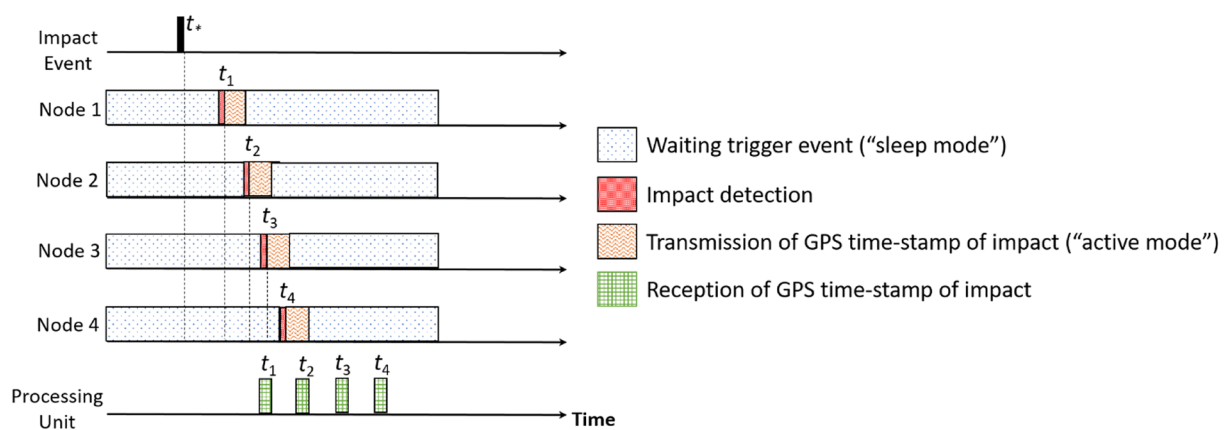


FIGURE 3 Illustration of the time synchronisation process with the GPS

various energy sources such as solar cells, batteries or energy harvesters. In this work, a 1000-mAh lithium polymer battery (LP553250) was used to feed each wire sensor node, which supports approximately 50 hr of autonomy assuming two detection events per day. Moreover, typical costs of WSN-based systems for SHM applications are in the range of \$50–\$100 per single node.³⁰ The proposed WSN has a cheap architecture, and it is expected that, for high-volume productions, costs will be in the lower end of the range.

3 | IMPACT LOCALISATION ALGORITHM

This section describes the mathematical model to retrieve the location of the AE source and the peak amplitude detection algorithm to estimate the TOA of propagating waves reaching each receiver wireless module.

3.1 | Analytical model

The impact localisation algorithm was originally developed by Ciampa and Meo,¹³ and it was recently improved by De Simone et al.² with a linearisation process of the system of nonlinear equations necessary to obtain the coordinates of the AE source and the velocity of propagating waves. With reference to Figure 4, the proposed impact localisation algorithm requires four PZT receiver transducers surface bonded on the test component. The receiver sensors are located at unknown distance $\|d_i\|$ ($i = 1, \dots, 4$) from the AE source and its planar Cartesian coordinates (x_{AE}, y_{AE}) are determined by solving the following system of nonlinear equations:

$$\begin{cases} \|d_i\| = \sqrt{(x_i - x_{AE})^2 + (y_i - y_{AE})^2} \\ t_i = \frac{\|d_i\|}{C_g} \end{cases}, \quad i = 1, \dots, 4, \quad (1)$$

where c_g is the velocity of propagating elastic waves reaching the i th sensor, t_i is the detection time (TOA) of AE signals and (x_i, y_i) are the known coordinates of the i th receiver transducer. Among different modes generated by the impact, the flexural A_0 Lamb wave was predominantly excited because of the point source exerting a pure out-of-plane force on the surface of the plate.^{13,43}

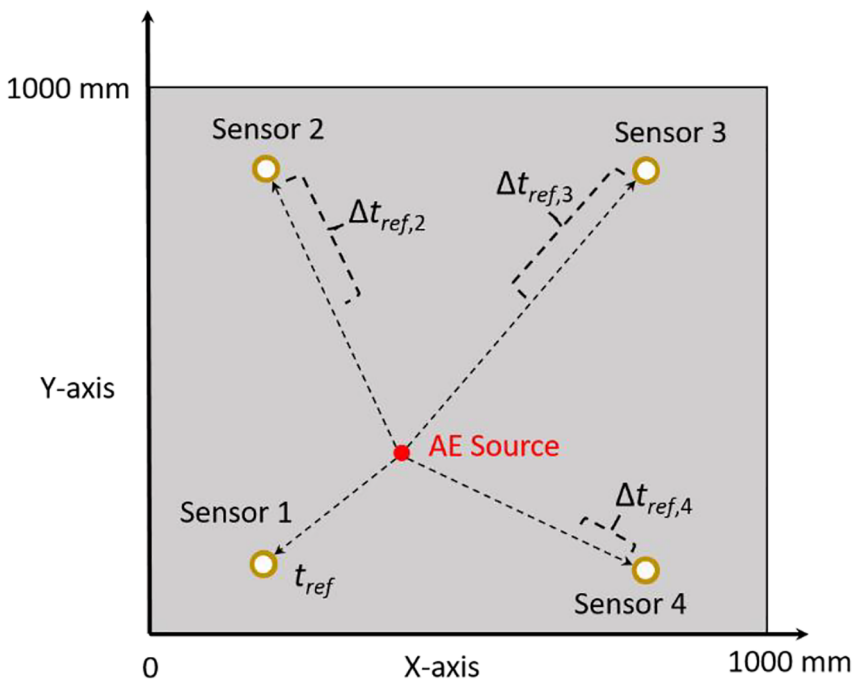


FIGURE 4 Illustration of the AE source location and receiver sensors position

Considering one of the sensors as the “reference sensor,” the following formula relates the travel time to reach the reference sensor, t_{ref} , with the time differences, $\Delta t_{\text{ref},j}$, between the reference sensor and the other receiver transducers:

$$t_j = t_{\text{ref}} \pm \Delta t_{\text{ref},j} \quad j = 1, \dots, 3. \quad (2)$$

Substituting Equation (2) into Equation (1), it leads to the following system of four nonlinear equations:

$$\begin{cases} (x_j - x_{\text{AE}})^2 + (y_j - y_{\text{AE}})^2 = [(t_{\text{ref}} \pm \Delta t_{\text{ref},j})c_g]^2, & j = 1, \dots, 3, \\ (x_{\text{ref}} - x_{\text{AE}})^2 + (y_{\text{ref}} - y_{\text{AE}})^2 = (t_{\text{ref}}c_g)^2 \end{cases} \quad (3)$$

which can be solved for the four unknowns (x_{AE} , y_{AE} , t_{ref} , c_g) by following the linearisation process reported in De Simone et al.² Each wireless node was designed to continuously acquire data from the ADC and seek for a signal sample crossing a predefined threshold (see Section 3.2). The time information, t_i , was obtained through a time synchronisation of the ADC sampling clock with a clock coherent with the GNSS signal available from the GNSS receiver. In particular, once the signal sample was detected, the wireless node switched from “sleep” to “active” mode allowing the MCU to acquire the GNSS time of that sample and send it to the central node through the radio channel.

3.2 | TOA estimation

The impact localisation algorithm presented in Section 3.1 relies on the TOA identification of ballistic waves traveling from the AE source to each individual wireless module. A number of time-frequency signal processing methods have been developed in the literature for the TOA estimation, including the wavelet transform,^{13,44} the cross-correlation method,⁴⁵ artificial neural networks,⁴⁶ and the Akaike information criterion.^{2,3} However, all these data-processing algorithms require advanced digital signal processing and large on-board storage capabilities of measured waveforms in order to extract AE features. The WSN here presented has purposely limited power resources and low processing capabilities so that a peak amplitude detection algorithm was used to analyse the AE data and estimate the TOA.⁴⁷ The peak amplitude detection algorithm converts measured time-domain signals into characteristic AE features once a predetermined threshold value is reached. In the proposed WSN, an edge trigger algorithm was used, in which the trigger was made in hardware by a simple comparator whose output signal is routed directly to the GNSS interrupt pin. As a result, the GNSS device provides the exact time instant when the trigger occurs. Moreover, in absence of a trigger event, the edge trigger algorithm enables the “sleep” mode of the MCU. With reference to the AE event reported measured by one of the wireless nodes (Figure 5), the signal detection is triggered by crossing the threshold condition (red dashed line). The wireless system was programmed to record all time instants when the threshold is crossed, including the time associated with the amplitude peak value. Indeed, additional AE features can be identified during the time interval between the first threshold crossing and the time when the AE waveform reaches its peak amplitude (known as the rise time). The peak amplitude

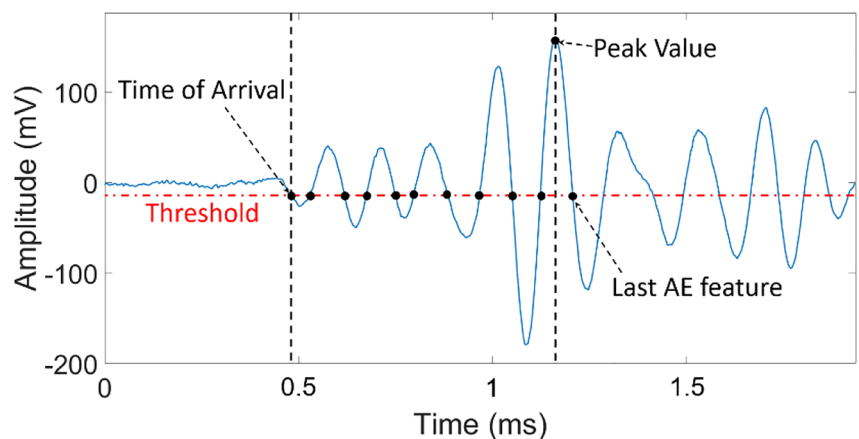


FIGURE 5 AE signal and its key features to estimate the TOA

determines the end of the acquisition of AE features, so that the last AE parameter is identified at the time instant when the AE signal crosses the threshold value after the amplitude peak.

It should be noted that the AE feature associated with the time instant of the first threshold crossing was here used for the TOA estimation. The time-stamp information provided during the threshold crossing is then transferred to the processing unit to localise the AE event. The “reference sensor” is automatically chosen by the WSN as one of the receiver sensors that experience the first threshold crossing between all wireless nodes. The AE features are finally recorded and transmitted to the processing unit.

4 | EXPERIMENTAL SET-UP

Impact localisation tests were performed to validate the proposed WSN by dropping a 10-mm diameter steel ball on the surface of an aluminium plate (Al 1050, 1,000 mm × 1,000 mm × 5 mm). Figure 6 illustrates the experimental set-up and the aluminium test component. Four piezo-sensors (PI 000041371), with piezo-electric coefficient values d_{31} , d_{33} , and d_{15} equal to -180×10^{-12} C/N, 400×10^{-12} C/N, and 550×10^{-12} C/N, respectively,⁴⁸ were bonded on the surface of the plate and connected to each single wireless node. The remote main node was then connected to the PC via a USB port to receive AE data from each wireless unit. The PC runs a MATLAB script developed by the authors, which receives the impact data from the peripheral sensors and estimates the impact location. Sensor locations are reported in Table 4, and the origin of the Cartesian reference frame for the impact localisation algorithm was located at the bottom left corner of the aluminium test sample.

5 | IMPACT LOCALISATION RESULTS AND DISCUSSIONS

In order to evaluate the performance of the proposed WSN system and the impact localisation algorithm reported in Sections 2 and 3, respectively, a number of low-velocity impacts was analysed. For the TOA estimation, only the AE

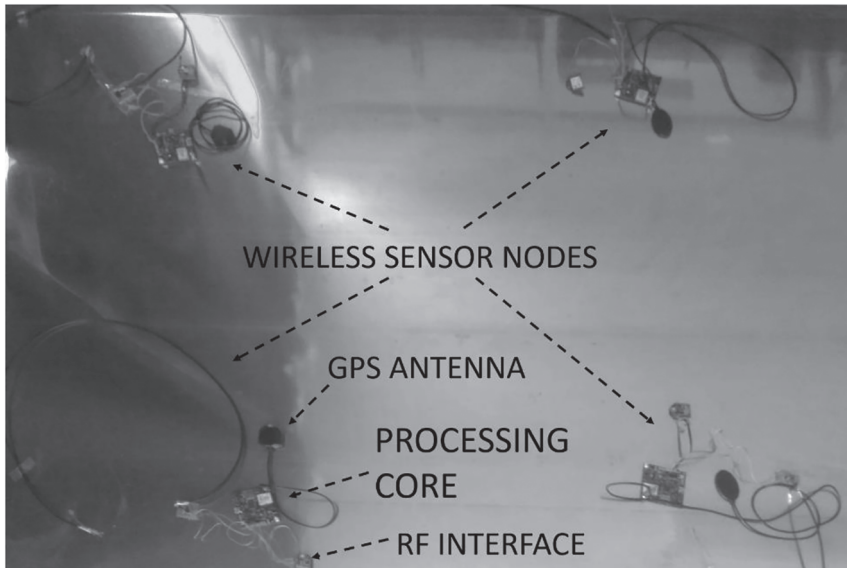


FIGURE 6 Illustration of wireless nodes location and the aluminium sample used during AE source localisation tests

TABLE 4 Sensors coordinates

	X-coordinate (mm)	Y-coordinate (mm)
Sensor 1	100	100
Sensor 2	100	900
Sensor 3	900	900
Sensor 4	900	100

feature associated with the time instant of the first threshold crossing was used. Figure 7 illustrates the impact localisation results in which the calculated impact points are represented as a red star (*) symbol, whereas the real impact points are shown as a green circle (O) symbol.

Table 5 reports the values of the real and calculated impact, the calculated time of the “reference sensor,” t_{ref} , the calculated wave speed of propagating ultrasonic waves, c_g , and the localisation error, ψ , as expressed by the following formula¹³:

$$\psi = \sqrt{(x_{\text{real}} - x_{\text{calculated}})^2 + (y_{\text{real}} - y_{\text{calculated}})^2}, \quad (4)$$

where x_{real} and y_{real} are the coordinates of the real impact point and $x_{\text{calculated}}$ and $y_{\text{calculated}}$ are the coordinates of the impact source using the proposed impact localisation algorithm.

As it can be seen from Table 5, the proposed WSN for impact localisation allowed achieving high accuracy in retrieving the coordinates of the AE source. The localisation error was not constant for all impact events but varied between ~ 5 mm and ~ 5 cm, with an average localisation error $\bar{\psi}$ equal to 24.56 mm. Such a variation of ψ can be associated to the time uncertainty caused by various sources of error affecting the impact localisation algorithm, including the accuracy of the GPS time, the ADC quantization error, the electronic noise of the analogue circuit, and the MCU elaboration time. For a more quantitative analysis, the total theoretical error on the position estimation, σ_P , can be calculated as the quadratic sum of all error contributes as follows:

FIGURE 7 Impact localisation results using the proposed WSN system. The calculated impact points are represented as a red star (*) symbol, whilst the real ones are shown as a green circle (O) symbol

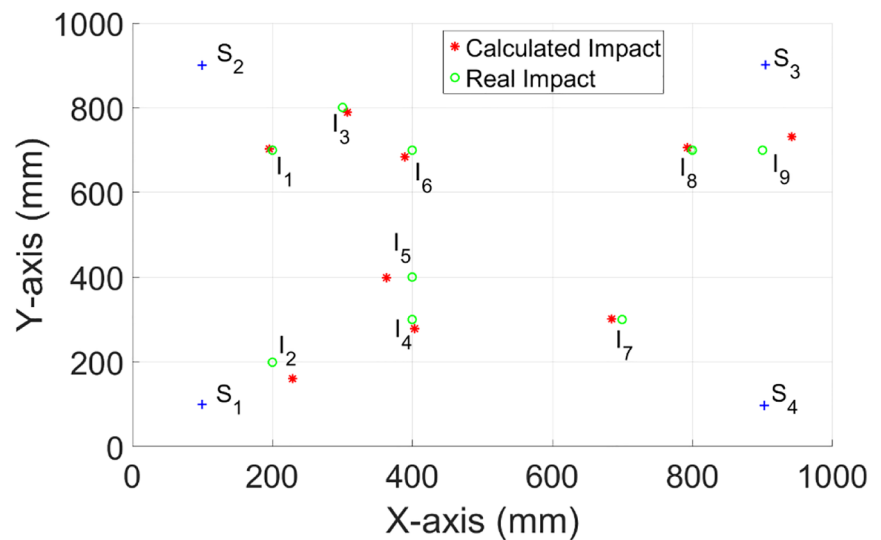


TABLE 5 Real and calculated impact coordinates (mm), calculated arrival time to the reference sensor (ms), calculated wave velocities (m/s), and localisation error (mm)

ID impact	x_{real} (mm)	y_{real} (mm)	$x_{\text{calculated}}$ (mm)	$y_{\text{calculated}}$ (mm)	t_{ref} (ms)	c_g (m/s)	Error ψ (mm)
I_1	200	700	196	702	0.178	1238	5
I_2	200	200	229	160	0.104	1291	49
I_3	300	800	307	789	0.184	1278	13
I_4	400	300	403	279	0.279	1261	21
I_5	400	400	363	398	0.321	1238	37
I_6	400	700	389	683	0.276	1311	20
I_7	700	300	685	302	0.285	1301	15
I_8	800	700	793	705	0.237	1199	9
I_9	900	700	942	731	0.149	1193	52

$$\sigma_P = \sqrt{4 \cdot c_g^2 \cdot (\sigma_{SF}^2 + \sigma_{ADC}^2 + \sigma_{GPS}^2 + \sigma_{MCU}^2)}, \quad (5)$$

where σ_{SF} ($\sim 4 \mu\text{s}$) is the time ambiguity due to the limited sampling frequency of 250 kHz and σ_{ADC} is the time uncertainty caused by the ADC non-idealities, i.e., the (a) clock jitter, (b) limited resolution, and (c) noise in the analogue front-end. Given the 100-kHz frequency bandwidth of acquired waveforms (the Nyquist frequency is 125 kHz), the signal-to-noise ratio (SNR) caused by the clock jitter in the ADC is given by.⁴⁹

$$SNR_{\text{jitter}_{ADC}} \approx -20 \log_{10}(2\pi \cdot 10^5 \cdot 50 \times 10^{-12}) \approx 90 \text{ dB}. \quad (6)$$

In Equation (6), the jitter period of 50 ps provided by the manufacturer (Microchip⁵⁰) was used. Since the SNR of the ADC due to the limited resolution, SNR_{ADC} , is 55 dB,⁵⁰ the effect of the clock jitter can be neglected. The full-scale voltage of the ADC, V_{FS} , is 3 V, and the noise of the ADC due to the limited resolution, v_{nADC} , can be calculated from the definition of SNR_{ADC} as follows,

$$v_{nADC} = \frac{V_{FS}}{SNR_{ADC}} = \frac{3 \text{ V}}{55 \text{ dB}} = \frac{3 \text{ V}}{562} \approx 5.3 \text{ mV}. \quad (7)$$

The noise in the analogue front-end, v_{nFE} , is obtained experimentally by measuring the noise of the system at rest and is approximately 40 mV. Therefore, the total noise is $v_n = \sqrt{v_{nADC}^2 + v_{nFE}^2} \approx 40.5 \text{ mV}$. By measuring experimentally the slew rate (SR) at the nominal frequency of 1 kHz ($SR = 6 \text{ V/ms}$), the time uncertainty caused by the ADC non-idealities, σ_{ADC} , is given by.⁵¹

$$\sigma_{ADC} = \frac{v_n}{SR} = \frac{40.5 \text{ mV}}{6 \frac{\text{V}}{\text{ms}}} \approx 7 \mu\text{s}. \quad (8)$$

It should be noted that the frequency of 1 kHz was chosen for the calculation of the SR as, in accordance with Figure 5, it provides the highest peak amplitude in the signal frequency spectrum. In Equation (5), σ_{GPS} ($\sim 100 \text{ ns}$) is the

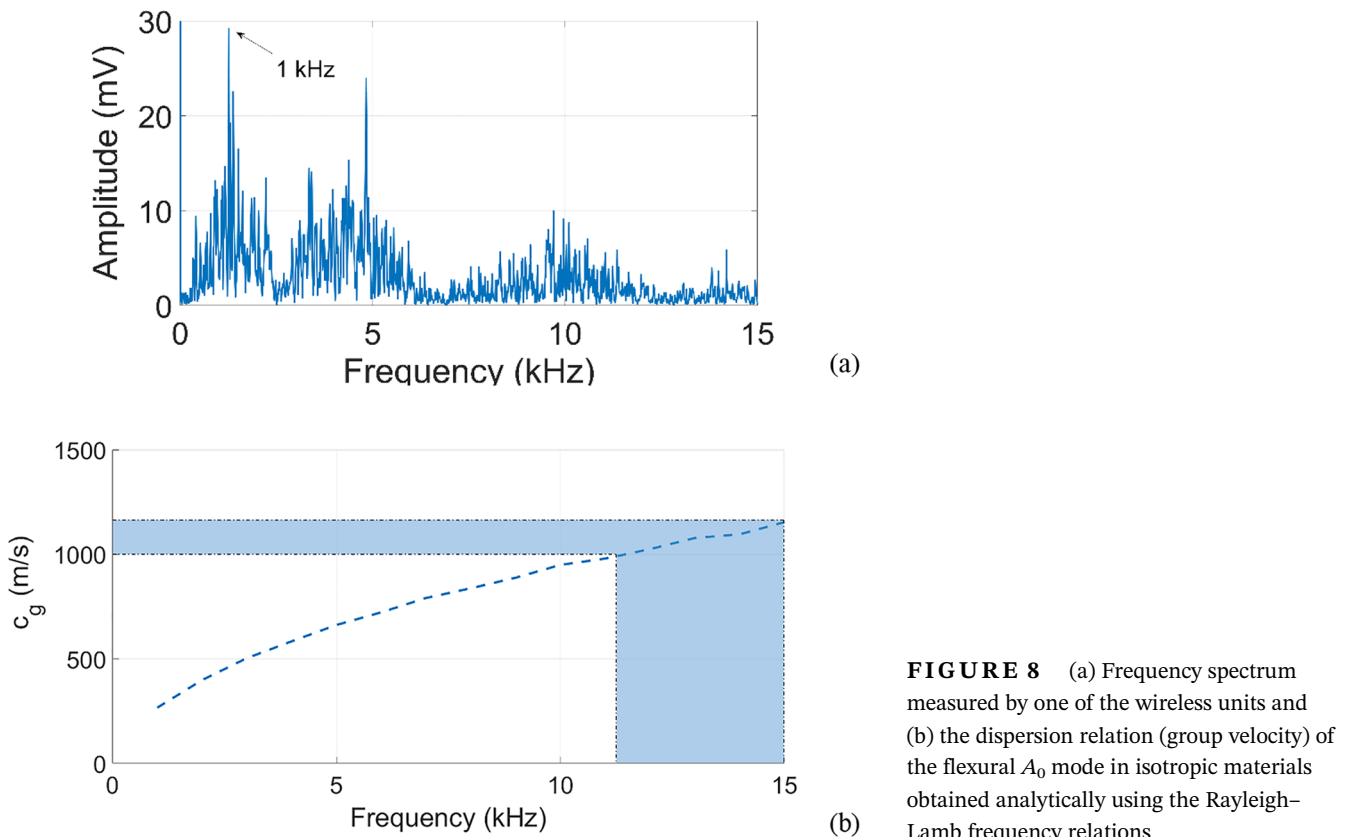


FIGURE 8 (a) Frequency spectrum measured by one of the wireless units and (b) the dispersion relation (group velocity) of the flexural A_0 mode in isotropic materials obtained analytically using the Rayleigh–Lamb frequency relations

time error due to the GPS time accuracy, and σ_{MCU} (~ 200 ns) is the measured time uncertainty due to the interrupt latency when the interrupt is at the maximum priority and the MCU clock is set at 100 MHz. Moreover, it can be seen from Equations (5), (7), and (8) that the main source of error is due to the limited sampling frequency and the analogue front-end noise. Hence, the localisation accuracy of the proposed WSN can be enhanced by simply adopting an ADC that samples signals at higher frequencies and by using a low-noise front-end. This would, however, affect costs of the single unit and the power demand. With reference to Equation (5) and Table 5, by considering an average calculated wave speed $\bar{c}_g = 1,257$ m/s and summing all these time error sources, the value of $\sigma_P = 20.27$ mm was obtained, which is comparable to the average localisation error $\bar{\psi} = 24.5$ mm. Furthermore, since the energy of each impact was constant, the order of magnitude of the ultrasonic wave velocity was very similar for all impact cases (see Table 5), with a standard deviation of ~ 40 m/s. The average value of the calculated wave speed, \bar{c}_g , was compared with the one obtained through the analytical approach using the Rayleigh–Lamb dispersion relations.⁵² With reference to Figure 8a, showing the frequency spectrum of one of signals measured by the wireless node, it can be seen that the signal spectrum is confined within the 0- to 15-kHz frequency range. By plotting the group velocity of the fundamental A_0 mode in this specific frequency range (Figure 8b), it can be observed that between 10 and 15 kHz, the group speed of the flexural Lamb mode is ranging between $\sim 1,000$ and 1,280 m/s. These values of the wave speed are very close to the average value of the velocity, \bar{c}_g , calculated by the impact localisation algorithm, thus further confirming the validity of the proposed WSN system.

6 | CONCLUSIONS

This paper proposed a low-power, low-weight, and low-cost WSN for the localisation of AE events on aircraft components. It consisted of a processing core module and a communication interface module for the RF transmission of recorded AE features. The processing core module included a 10-bit ADC, a GNSS receiver for accurate time synchronisation, a micro SD slot, a USB 2.0 interface, and a 32-bit MCU that enabled the low-power “sleep” mode. These components were chosen consistently to meet low-power requirements with a maximum weight of ~ 30 g. The total power consumption was ~ 80 mW when no AE signals were detected and ~ 360 mW in order to transmit the AE features for few milliseconds to a remote central unit. A localisation algorithm based on the TOA estimation was used to retrieve the coordinates of the impact location and the speed of flexural propagating waves. A simple peak amplitude detection system was implemented to extract the AE time features. Experimental results on an aluminium plate revealed that the impact location could be estimated with high level of accuracy, with a maximum average localisation error of about 2 cm. A quantitative analysis of the theoretical error on the position estimation also showed that such a localisation error could be minimised by using high performing and costly ADC. Moreover, good agreement was found between the group speed measured by the localisation algorithm and that obtained using theoretical dispersion relations.

Future work is ongoing to integrate all the hardware in a single board, thus making the proposed WSN more compact, flexible, and portable. Moreover, given the low-power consumption of the proposed wireless system, energy harvesting technologies could replace batteries and enable each node functioning in remote locations and real operating scenarios.

CONFLICT OF INTEREST

The author(s) declared no potential conflicts of interest with respect to the research, authorship, and/or publication of this article.

ORCID

Carmine Gianni  <https://orcid.org/0000-0001-9454-1577>

Marco Balsi  <https://orcid.org/0000-0002-3571-2353>

Salvatore Esposito  <https://orcid.org/0000-0001-6610-6498>

Francesco Ciampa  <https://orcid.org/0000-0003-3846-8891>

REFERENCES

1. Diamanti K, Soutis C. Structural health monitoring techniques for aircraft composite structures. *Progress in Aerospace Sci.* 2010;46(8): 342-352.

2. De Simone M, Ciampa F, Boccardi S, Meo M. Impact source localisation in aerospace composite structures. *Smart Mat Struct.* 2017;26(12):125026.
3. Pearson MR, Eaton M, Featherston C, Pullin R, Holford K. Improved acoustic emission source location during fatigue and impact events in metallic and composite structures. *Struct Health Monit.* 2017;16(4):382-399.
4. Matt HM, di Scalea FL. Macro-fiber composite piezoelectric rosettes for acoustic source location in complex structures. *Smart Mat Struct.* 2007;16(4):1489.
5. Salmanpour MS, Sharif Khodaei Z, Aliabadi MH. Impact damage localisation with piezoelectric sensors under operational and environmental conditions. *Sensors.* 2017;17(5):1178.
6. Kundu T. Acoustic source localization. *Ultrasonics.* 2014;54(1):25-38.
7. Tobias A. Acoustic-emission source location in two dimensions by an array of three sensors. *Nondest Test Eval Int.* 1976;9:9-12.
8. Kundu T, Das S, Jata KV. Point of impact prediction in isotropic and anisotropic plates from the acoustic emission data. *J Acoust Soc Am.* 2007;122(4):2057-2066.
9. Kundu T, Das S, Martin SA, Jata KV. Locating point of impact in anisotropic fiber reinforced composite plates. *Ultrasonics.* 2008;48(3):193-201.
10. Michaels J-E, Michaels T-E. Guided wave signal processing and image fusion for in situ damage localization in plates. *Wave Motion.* 2007;44:482-492.
11. Michaels J-E, Michaels T-E. Damage localization in inhomogeneous plates using a sparse array of ultrasonic transducers. *AIP Conf Pro.* 2007;894:846-853.
12. Gao H, Shi Y, Rose J. Guided wave tomography on an aircraft wing with leave in place sensors. *AIP Conf Proc.* 2005;760:1788-1794.
13. Ciampa F, Meo M. Acoustic emission source localization and velocity determination of the fundamental mode A_0 using wavelet analysis and Newton-based optimization technique. *Smart Mat Struct.* 2010;19:1-14.
14. Ciampa F, Boccardi S, Meo M. Factors affecting the imaging of impact location with inverse filtering and diffuse wave fields. *J Intel Mat Syst Struct.* 2016;27(11):1523-1533.
15. Ciampa F, Meo M. Impact location on a composite tail rotor blade using an inverse filtering approach. *J Intel Mat Syst Struct.* 2014;25(15):1950-1958.
16. Ciampa F, Meo M. Acoustic emission localization in complex dissipative anisotropic structures using a one-channel reciprocal time reversal method. *J Acoust Soc Am.* 2011;130(1):168-175.
17. Ebrahimkhanlou A, Salamone S. Acoustic emission source localization in thin metallic plates: a single-sensor approach based on multi-modal edge reflections. *Ultrasonics.* 2017.
18. Heinen, H. The A380 program, *Global Investor Forum*, 2006.
19. Lédeczi Á, Hay T, Volgyesi P, Hay DR, Nádás A, Jayaraman S. Wireless acoustic emission sensor network for structural monitoring. *IEEE Sensors J.* 2009;9(11):1370-1377.
20. Saric ZM, Kukulj DD, Teslic ND. Acoustic source localization in wireless sensor network. *Circ Sys Signal Proc.* 2010;29(5):837-856.
21. Chen Z. Energy efficiency strategy for a general real-time wireless sensor platform. *Smart Struct Syst.* 2014;14(4):617-641.
22. Winter BD, Swartz RA. Wireless structural control using multi-step TDMA communication patterning bandwidth allocation. *Struct Control Health Monit.* 2017;24(12):e2025.
23. Straser EG, Kiremidjian AS. Modular wireless damage monitoring system for structures, Report No. 128, John A. Blume Earthquake Engineering Center, Department of Civil and Environmental Engineering, Stanford University, Stanford, CA, 1998.
24. Bennett, R., Hayes-Gill, B., Crowe, J.A., Armitage, R., Rodgers, D. and Hendroff, A. Wireless monitoring of highways. In *Smart Structures and Materials 1999: Smart Systems for Bridges, Structures, and Highways* (Vol. 3671, pp. 173-182). International Society for Optics and Photonics, 1999.
25. Casciati S, Chen Z. A multi-channel wireless connection system for structural health monitoring applications. *Struct Control Health Monit.* 2011;18(5):588-600.
26. Chen Z, Casciati F. A low-noise, real-time, wireless data acquisition system for structural monitoring applications. *Struct Control Health Monit.* 2014;21(7):1118-1136.
27. Samson D, Kluge M, Becker T, Schmid U. Wireless sensor node powered by aircraft specific thermoelectric energy harvesting. *Sensors and Actuators a: Physical.* 2011;172(1):240-244.
28. Scarselli G, Nicassio F, Pinto F, Ciampa F, Iervolino O, Meo M. A novel bistable energy harvesting concept. *Smart Mat Struct.* 2016;25(5):055001.
29. Lynch JP, Loh KJ. A summary review of wireless sensors and sensor networks for structural health monitoring. *Shock and Vibration Digest.* 2006;38(2):91-130.
30. Aygün B, Cagri Gungor V. Wireless sensor networks for structure health monitoring: recent advances and future research directions. *Sensor Rev.* 2011;31(3):261-276.
31. Chen S, Dong X, Kim JY, Wu S, Wang Y. Design and performance validation of a compact wireless ultrasonic device for localized damage detection. *Adv Struct Eng.* 2016;19(2):270-282.
32. Liu P, Yuan S, Qiu L. Development of a PZT-based wireless digital monitor for composite impact monitoring. *Smart Mat Struct.* 2012;21(3):035018.
33. Yuan S, Mei H, Qiu L, Ren Y. On a digital wireless impact-monitoring network for large-scale composite structures. *Smart Mat Struct.* 2014;23(8):085007.

34. Becker T, Kluge M, Schalk J, et al. Autonomous sensor nodes for aircraft structural health monitoring. *IEEE Sensors J.* 2009;9(11):1589-1595.
35. Bouzid OM, Tian GY, Cumanan K, Moore D. Structural health monitoring of wind turbine blades: acoustic source localization using wireless sensor networks. *J Sensors.* 2015;2015:1-11.
36. Casciati F, Casciati S, Chen Z, Faravelli L, & Vece M. Collecting data from a sensor network in a single-board computer. In *Journal of Physics: Conference Series* (Vol. 628, No. 1, p. 012113). IOP Publishing, 2015.
37. Meo M, Zumpano G. On the optimal sensor placement techniques for a bridge structure. *Eng Struct.* 2005;27(10):1488-1497.
38. Wu L, Casciati F. Local positioning systems versus structural monitoring: a review. *Struct Control Health Monit.* 2014;21(9):1209-1221.
39. Shen G, Zhang Y, Dong Y, Liu S. Development of high-speed Wi-Fi wireless acoustic emission system. In: *Advances in Acoustic Emission Technology*. New York: Springer; 2015:3-13.
40. Yedavalli RK, Belapurkar RK. Application of wireless sensor networks to aircraft control and health management systems. *JControl Theory Appl.* 2011;9(1):28-33.
41. Garcia GJ, Jara CA, Pomares J, Alabdo A, Poggi LM, Torres F. A survey on FPGA-based sensor systems: towards intelligent and reconfigurable low-power sensors for computer vision, control and signal processing. *Sensors.* 2014;14(4):6247-6278.
42. Jurdak R, Ruzzelli AG, O'Hare GM. Radio sleep mode optimization in wireless sensor networks. *IEEE Trans Mobile Comp.* 2010;9(7):955-968.
43. Clarke T, Simonetti F, Rohklin S, Cawley P. Development of a low-frequency high purity A0 mode transducer for SHM applications. *IEEE Trans Ultrason Ferroelectr Freq Control.* 2009;56(7):1457-1468.
44. Ciampa F, Meo M, Barbieri E. Impact localization in composite structures of arbitrary cross section. *Struct Health Monit.* 2012;11(6):643-655.
45. Ziola SM, Gorman MR. Source location in thin plates using cross-correlation. *J Acoust Soc Am.* 1991;90(5):2551-2556.
46. Dai H, MacBeth C. The application of back-propagation neural network to automatic picking seismic arrivals from single-component recordings. *J Geophys Res Solid Earth.* 1997;102(B7):15105-15113.
47. Marioli D, Narduzzi C, Offelli C, Petri D, Sardini E, Taroni A. Digital time-of-flight measurement for ultrasonic sensors. *IEEE Trans Instrument Measure.* 1992;41(1):93-97.
48. Carrino S, Nicassio F, Scarselli G. Nonlinearities associated with impaired sensors in a typical SHM experimental set-up. *Electronics.* 2018;7(11):303.
49. Azeredo-Leme C. Clock jitter effects on sampling: a tutorial. *IEEE Circuits and Sys Mag.* 2011;11(3):26-37.
50. Datasheet, M. PIC32MX330 Data Sheet 32-bit Microcontrollers. online: www.microchip.com.
51. Maxim Integrated Products: Application Note 3631, "Random Noise Contribution to Timing Jitter—Theory and Practice", available at <http://www.maximintegrated.com/an3631>, 2005.
52. Viktorov IA. *Rayleigh and Lamb Waves: Physical Theory and Applications*. New York: Plenum; 1967.

How to cite this article: Giannì C, Balsi M, Esposito S, Ciampa F. Low-power global navigation satellite system-enabled wireless sensor network for acoustic emission localisation in aerospace components. *Struct Control Health Monit.* 2020;27:e2525. <https://doi.org/10.1002/stc.2525>